UC Berkeley
UC Berkeley Previously Published Works

Title

Impact of Salt Concentration on Nonuniform Lithium Electrodeposition through Rigid Block Copolymer Electrolytes

Permalink

https://escholarship.org/uc/item/0211g01p

Journal

ACS Applied Materials & Interfaces, 11(51)

ISSN

1944-8244

Authors

Frenck, Louise
Maslyn, Jacqueline A
Loo, Whitney S
et al.

Publication Date

2019-12-26

DOI

10.1021/acsami.9b15606

Peer reviewed

Impact of Salt Concentration on Non-uniform Lithium Electrodeposition through Rigid Block Copolymer Electrolytes

Louise Frenck[a,b], Jacqueline A. Maslyn[a,b], Whitney S. Loo[a], Dilworth Y. Parkinson[c], Nitash P. Balsara[a,b*]

[a]Department of Chemical and Biomolecular Engineering, University of California, Berkeley, California 94720, United States

[b]Materials Sciences Division, Lawrence Berkeley National Laboratory, Berkeley, California 94720, United States

[c]Advanced Light Source, Lawrence Berkeley National Laboratory, Berkeley, California 94720, United States

ABSTRACT: There is a growing demand for higher energy density lithium batteries. One approach for addressing this demand is enabling lithium metal anodes. However, nucleation and growth of electronically conductive protrusions which cause short circuits prevent the use of this technology with liquid electrolytes. The use of rigid solid electrolytes such as polystyrene-*b*-poly(ethylene) oxide electrolytes is one solution. An additional requirement for practical cells is need to use electrolytes with high salt concentration to maximize the flux of lithium ions in the cell. The first systematic of the effect of salt concentration on the morphology of electrodeposited lithium through a rigid block copolymer electrolyte is presented. The nature, areal density, and morphologies of defective lithium deposits created during galvanostatic cycling of lithium-lithium symmetric cells, were determined using hard X-ray microtomography. Cycle life decreases rapidly with increasing salt concentration. X-ray microtomography reveals the presence of multi-globular protrusions which are nucleated at impurity particles at low salt concentrations; the areal of defective lithium deposits was independent salt concentration. At the highest salt concentration, this density increases abruptly by a factor of about 10, and defects were also nucleated at locations where no impurities were visible.

INTRODUCTION

High energy density batteries are necessary to enable a sustainable and clean energy network, and also electrification of transportation[1,2]. In this context, lithium metal anodes are of considerable current interest due to its high theoretical capacity $(3,860 \text{ mAh.g}^{-1})$[3], low atomic mass, and high electropositivity[4]. Since the first lithium metal battery made by Whittingham *et al.*[5], there has been increased motivation to understand the redox behavior of lithium metal. Lithium metal batteries exhibit premature failure due to nonplanar electrodeposition of lithium ions during charging of the battery leading to catastrophic failure by short circuit causing safety issues.[3,6-8] Despite its attractive properties, lithium reacts with liquid electrolytes used currently in rechargeable batteries,[3,7,9] leading to low coulombic efficiency and active consumption of electrolyte[3]. Following the discovery of the solvation of alkali metals in poly(ethylene oxide) (PEO) by Fenton *et al.*[10], Armand *et al.*[11] demonstrated that PEO-based electrolytes can be used in rechargeable lithium metal batteries. Several studies on solid polymer electrolytes show improved stability against lithium metal.[12-15] In practical batteries, electrolytes with high salt concentrations must be employed to maximize the flux of the active lithium ions. To our knowledge, there are no systematic studies of the effect of salt concentration on the nature of the electrochemical deposition of lithium metal. Our purpose is to present an experimental study of this effect. In particular, we demonstrate new electrodeposition modes at high salt concentration gradients.

A major problem with lithium metal batteries is dendritic growth during charging.[16-18] Monroe and Newman[19-21] predicted the suppression of dendrites

for electrolytes having twice the shear modulus of lithium metal, motivating the use of block copolymer electrolytes with co-continuous rigid domains that control the electrolyte mechanical properties and soft rubbery domains that provide avenues for ion transport. We used a well-studied block copolymer electrolyte, polystyrene-*block*-poly(ethylene oxide) (PS-*b*-PEO or SEO), [22-30] to examine the effect of salt concentration on electrodeposition.

The electrolyte was subjected to galvanostatic cycling in lithium-lithium symmetric cells. The nature of lithium deposition in the cells was determined by hard X-ray microtomography. We were able to determine the nature, the density, and the morphologies of defective lithium created by electrodeposition for a wide range of salt concentrations. The defects that we found were either globular protrusions or mossy lithium deposits. The work presented here builds on previous studies where we studied the effect of temperature[31] and current density[30] on electrodeposition of lithium through block copolymer electrolytes.

EXPERIMENTAL SECTION

Materials. The samples discussed in this study were prepared using the following techniques. A polystyrene-*block*-poly(ethylene oxide) copolymer electrolyte (SEO) was prepared by anionic polymerization, as described in previous work[32-34]. The molar mass of PS and PEO blocks were 235 and 222 kg.mol^{-1}, respectively, with a PEO volume fraction of 0.475 without salt and an overall polydispersity index of 1.05. The morphology of the block copolymer is lamellar, consistent with the PEO volume fraction[35,36] and the calculated domain spacing is $d = 130$nm according to the strong segregation limit theory. Methods for electrolyte preparation and electrochemical cycling mimics those previously reported by Maslyn *et al.*[27-30]. All electrolyte preparation and lithium cell assembly steps were performed in an Argon filled glovebox with less than 1 ppm of water and less than 1 ppm of oxygen.

Electrolyte preparation. SEO block copolymer was dissolved in anhydrous *N*-methylpyrrolidone (NMP, from Sigma Aldrich) and mixed with bis(trifluoromethane) sulfonimide lithium salt (LiTFSI) (purchased at Novalyte), which was dried for 3 days at 120 °C under active vacuum prior to use. The molar ratio of lithium ions to ethylene oxide groups (r), also called salt concentration, varied from 0.04 to 0.2 (r = 0.04, 0.06, 0.085, 0.10, 0.12, 0.15, 0.18, 0.20). An electrolyte film was then cast on a nickel-foil-coated solvent caster to form a 50 μm-thick membrane after the NMP evaporated away after 12 hours at 60 °C. The membrane formed was then further dried under active vacuum at 90 °C for at least 48 hours; then, dried electrolytes were brought inside an Argon filled glove box where all the cell assembly took place.

Li-SEO-Li Symmetric Cell Assembly for Cycling and Tomographic Imaging. Lithium-lithium symmetric cells were assembled as described in reference [30]. All cells were vacuum sealed in polypropylene-lined aluminum pouch material in order to conduct further experiments outside the glovebox.

Conditioning and Cycling. All experiments were run at 90ºC. Galvanostatic conditioning cycles were performed as described in reference [30]. After conditioning cycling ata current density i = 0.02mA.cm^{-2}, cells were then cycled with the same procedure, but with the current density of interest, 0.175 mA.cm^{-2}. For those cycles, the new thickness of lithium plated or stripped between the electrodes in each half cycle was 3.4 μm. For each salt concentration, 3 to 6 cells were cycled and analyzed.

X-ray Microtomography. Beamline 8.3.2 at the Advanced Light Source at Lawrence Berkeley National Laboratory was used to perform hard X-ray microtomography experiments. The cells were imaged using the apparatus described in [30]. For consistency, the electrode stripped during the first half of the first cycle (and the first half of subsequent cycles) is shown on top in all tomography images.
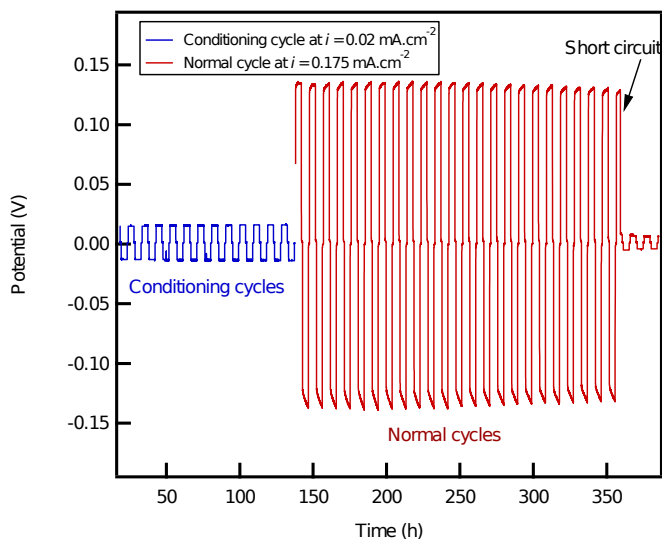
RESULTS AND DISCUSSION

Figure 1. Typical voltage versus time profile of a lithium-lithium symmetric cell that was galvanostatically cycled. Conditioning cycles at i = 0.02 mA.cm^{-2}, are represented in blue, while normal cycling at i = 0.175 mA.cm^{-2}, is represented in red. The sudden drop in potential seen at t =350 h is indicative of a short circuit failure due to the growth of lithium protrusions.

Figure 1 shows typical voltage versus time data for galvanostatic cycling of a lithium-lithium symmetric cell. First, the cell was conditioned at low current density, i, (0.02 mA.cm^{-2} in blue) for 15 cycles. We have found that this step is necessary to obtain consistent data from different cells; we believe that this is due to stabilization of the electrolyte-electrode interfaces and the formation of the solid electrolyte interphase (SEI)[37]. We note that the voltage is fairly stable from the first cycle to the 15th

one during conditioning, demonstrating a stable bulk and interfacial impedance. This also suggests that nucleation and growth of lithium protrusions is completely suppressed during the conditioning step[30]. After completing the conditioning step, the cell is cycled at the current density of interest, i.e. i = 0.175 mA.cm^{-2} (in red). All the cells studied were cycled until failure. In most cases, the voltage suddenly dropped to a value close to zero, a signature of a direct short circuit due to the formation of a lithium protrusion that crosses the cell. In a 2 out of 31 cells, the voltage drop was sudden but less severe. We define the cell lifetime as the time at which a sudden drop in voltage was observed. As seen in Figure 1, there are no significant changes in the potential before the short. Therefore, it is not possible to forecast the time of the short based on potential measurements.
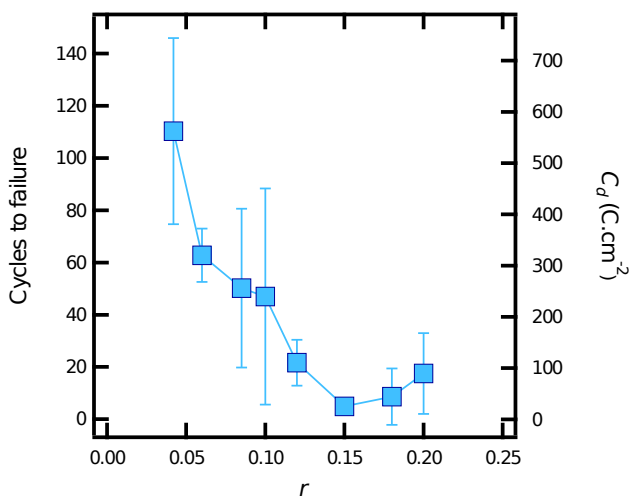

Figure 2. Average number of cycles to failure and charge density passed, before failure, C_d, as a function of salt concentration, r. The conditioning cycles are not taken into account. The right ordinate shows the charge density passed before failure, including charge passed during conditioning cycles (8.64 C.cm^{-2}), calculated from the number of cycles to failure.

The experiments described in Figure 1 were repeated on a total of 31 cells that cover a salt concentration range $0.04 \leq r \leq 0.2$. For each salt concentration, the average values of the total number of cycles before failure were determined and the results are plotted in Figure 2. Each average was taken from 3 to 6 cells. The total number of cycles to failure was defined as full cycles from the first cycle at 0.175 mA.cm^{-2}, excluding the 15 first conditioning cycles. The errors bars represent the standard deviation for each data set. The left axis of the plot gives the number of cycles before failure, while the right axis of the plot converts the number of cycles into a charge density passed, C_d, including the 15 conditioning cycles (8.64 C.cm^{-2}). The charge passed before failure is calculated using the time of failure and the imposed current density. Cell failure is a complicated process that depends on many factors including the distribution of impurities in the

lithium metal electrodes, imperfect cell assembly, the stochastic nature of lithium protrusion nucleation, the lack of controlled pressure during cycling (the nominal pressure is 1 atm due to the vacuum inside the pouch), and unavoidable variations in local electrolyte thickness. The standard deviation of C_d values in Figure 2 is thus not entirely surprising.

In spite of the scatter of the data, Figure 2 shows a clear and surprising trend: the cell lifetime decreases rapidly with increasing salt concentration until a minimum is reached at r = 0.15. At low salt concentration for cells with r = 0.04, the average charge passed is 565 C.cm^{-2} (110 cycles), while for high salt concentration for cells with r = 0.15, the average charge passed is only 33 C.cm^{-2} (5 cycles). After the minimum at r = 0.15, cell lifetime slightly increases, from 33 to 97 C.cm^{-2} from r = 0.15 to r = 0.2 (17 cycles). This difference in cell lifetime is well outside of experimental uncertainty. Therefore, we conclude that the ability of SEO to withstand the effects of dendrites decreases dramatically with increasing salt concentration. Since concentrated electrolytes are needed for practical applications, this result is of significant practical interest.

In order to gain insight into the nature of the shorts which lead to cell failure, X-ray microtomography was performed on the conditioned (before cycling) and the failed cells (after cycling). Figure 3 shows a typical cross-section of the reconstructed data for a cell after conditioning cycles. The tomogram is divided in 3 distinct regions: on the top and bottom, the dark grey pixel values represent lithium electrodes, while the bright band in the center represents the electrolyte. The grayscale pixel values reflect the linear X-ray absorption coefficient of the material: the higher the pixel value (i.e. the brighter the pixel), the higher the absorption coefficient of the material. Lithium metal has the smallest absorption coefficient[38] due to its small atomic number (3): therefore, it is more X-ray transmittive and appears darker. Imaging samples containing interfaces leads to the presence of Fresnel phase contrast[39,40], which is visible in the tomograms at the electrode-electrolyte interface as a thin dark band on the electrode side and a thin bright band on the electrolyte side. It is important to note that the Fresnel phase contrast affects all interfaces including those formed when lithium deposition is non-uniform. After conditioning, cells do not exhibit any noticeable features (Figure 3). We imaged a total of 6 cells after conditioning, mainly cells with medium and high salt concentration (r = 0.12 to 0.2), and we found no evidence of defective lithium deposition during this step[30]. Figure 3 also shows excellent adhesion between the electrodes and the electrolyte. On the top right of the tomogram in Figure 3, a bright particle can be observed inside the lithium electrode. This is a large crystalline impurity lying within the lithium metal bulk. Numerous smaller crystalline impurities are present, and they are randomly distributed within the lithium electrode. [27–31]
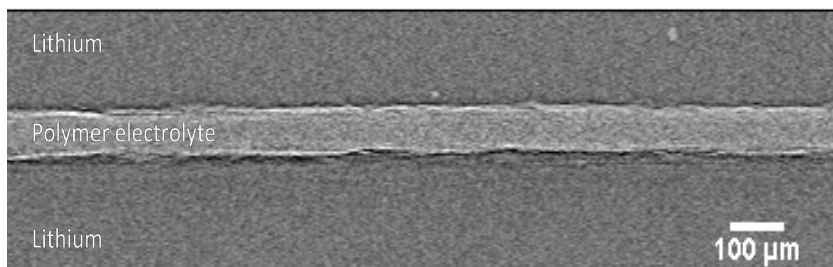
Figure 3. Cross-sectional slice through the reconstructed X-ray tomogram of a lithium metal/ polymer electrolyte/lithium metal symmetric cell after the passage of current for conditioning cycles at $i = 0.02$ mA.cm^{-2}. The polymer electrolyte membrane appears as a light and unbroken band separating the two lithium metal electrodes. No lithium protrusions were observed in any symmetric cells after conditioning cycles.

Figure 4 shows a reconstructed X-ray tomography slice through the volume of the lithium foil containing many impurity particles. Faceted impurity particles of different sizes (from 9 to 37 µm) and shape (triangles, diamonds, etc.) are evident. Moreover, they are brighter than lithium indicating higher electron density. Previous Energy dispersive X-ray spectroscopy (EDS) studies[28] indicate that these impurity comprise either lithium oxide (Li_2O), lithium hydroxide (LiOH) or lithium nitride (Li_3N). It is important to note that those impurities are by their nature electronic insulators.
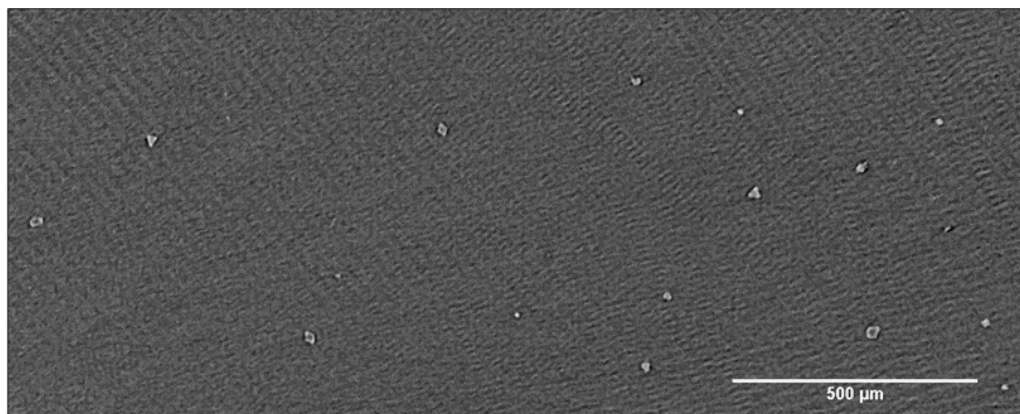

Figure 4. Reconstructed X-ray tomography slice into the volume of lithium showing the presence of impurity particles embedded into the lithium foil. Impurity particles appear brighter than lithium and have faceted shape. This slice was obtained from an uncycled cell, and is parallel to and 100 µm away from the lithium-SEO interface.

Typical X-ray tomography results from cycled and failed cells are shown in Figure 5 a,b,d,e. Non-uniform plating was observed in both top and bottom electrode. By definition, the top electrode is the one that was stripped first during the 0.175 mA.cm^{-2} cycling first step. For consistency all the protrusions shown in Figure 5 are nucleated from the top electrode. Similar protrusions were found in all cells regardless of salt concentration. Figure 5a shows a typical protrusion found at the electrode-electrolyte interface after cell cycling. Those objects are composed of globular clusters, which is consistent with protrusion morphologies already reported for similar SEO electrolytes[27–29,31]. In addition, we observed the presence of a crystalline impurity at the protrusion's foot. The pixels within the cluster are different from pure lithium or pure electrolyte suggesting that the globules contain lithium, salt, and SEO. The higher brightness of the object is partly due to the phase contrast but can also be coming from a higher X-ray absorption coefficient. One hypothesis is the presence of a salt rich phase inside those objects. The globular structures in Figure 5a span the electrode-electrolyte interface. Figure 5b presents a top view of the same dendrite shown in (a) (xy plane shown as a dashed line in Figure 5a; this portion of the globular structure is located inside the polymer electrolyte. The dark pixels represent globules of lithium; the globules appear darker than bulk lithium foil due to Fresnel bands. The bright pixels represent the polymer electrolyte. The multiglobular nature of this object is clear. Small globules of non-planar lithium are punctured an electrolyte-rich phase. Globule size varies from 8 to 24 µm. In the globular structure shown in Figure 5a,b, the center is mainly composed of polymer electrolyte (bright pixels).

Figure 5d presents a typical protrusion structure spanning the electrolyte, which caused the failure of the cell. The structure is very similar to the one presented in Figure 5a; however, we can clearly see the dark lithium pixels crossing the electrolyte from the top to the bottom electrode. Figure 5e shows the top view of the cell-spanning structure in Figure 5d. Here, we can observe that the lithium globules have dimensions from 22 to 56 µm, somewhat larger than those see in Figure 5b. The lithium globules are

connected to each other in the electrolyte-spanning cluster (Figure 5e) but not in the cluster largely confined to the top electrode (Figure 5b). In addition, the electrolyte spanning cluster is dominated by lithium, while the non-spanning cluster has both lithium and electrolyte in it.
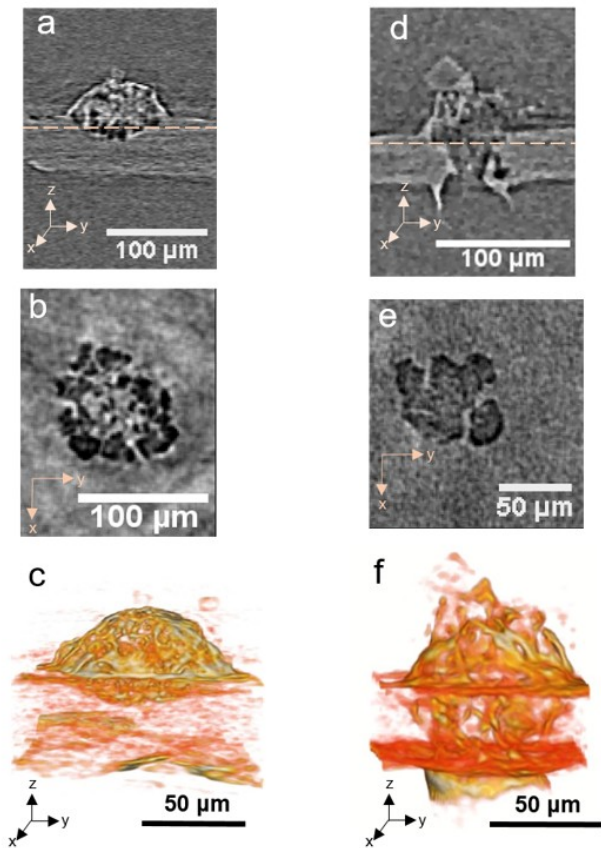

Figure 5**.** Examples of non-planar lithium electrodeposition observed in this study by X-ray tomography. Orthogonal cross-sections through the cell and the defect are presented on the top row. The middle row presents a top view of the same structure from the plane indicated by the orange dashed line shown in the top row. 3D visualizations that includes the defect, are presented on the bottom row. (a) Cross-section in the yz plane of a multiglobular defect not spanning the electrolyte. (b) Cross-section in the xy plane of the defect shown in (a). (c) Volume rendering of the defect shown in (a) and (b). (d) Cross-section in the yz plane of a multiglobular defect spanning the electrolyte and shorting the cell. (e) Cross-section in the xy plane of the defect shown in (d). (f) Volume rendering of the defect shown in (d) and (e). (a) to (c) were obtained from a cell with $r = 0.02$ and (d) to (f) were obtained from a cell with $r = 0.042$. These types of objects were found for the whole range of salt concentration.

3D volume renderings through the cell are created by stacking slices of the type shown in Figures 5a, 5b, 5d, and 5e. Visualizations of these volume renderings are shown in Figures 5c and 5f. The color scheme of the visualizations is based on the grayscale values of the voxels: all voxels below a certain threshold brightness value were rendered transparent and the remaining voxels were placed on a color scale ranging from red to yellow. Red indicates the least bright visible voxels, orange indicates voxels of intermediate brightness values, and yellow indicates the brightest visible voxels. The volume rendering helps visualize the nature of the polymer/salt phase that surrounds the lithium globules. Figure 5c and Figure 5f show the three dimensional structure of the electrolyte phase that surrounds the lithium globules. This phase is like a sac that contains the lithium globules. The sac is ruptured in the system-spanning cluster. Also seen in Figure 5c,f are the crystalline impurities that nucleated the cluster.
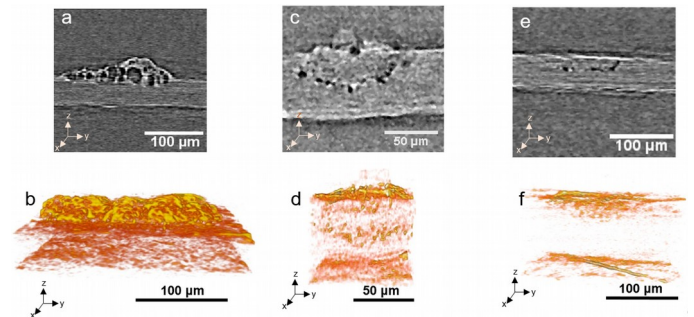

Figure 6. Examples of non-planar lithium electrodeposition observed in this study by X-ray tomography for cells with the highest salt concentration, $r = 0.2$. Orthogonal cross-sections through the defect are presented on the top row. 3D visualizations that includes the defect, are presented on the bottom row. (a) and (b) Multiglobular defect not spanning the electrolyte nucleated without crystalline impurity, (c) and (d) mossy lithium nucleated from a crystalline impurity, and (e) and (f) mossy lithium without crystalline impurity.

The globular clusters depicted in Figure 5 were seen at all salt concentrations. However, three other types of defective lithium deposits were observed only in cells with the highest salt concentration, $r = 0.2$, and they are presented Figure 6 a to f. The top figures are cross sectional slices of dendritic objects (Figure 6a,c,e), while the bottom figures are 3D volume renderings of those objects (Figure 6b,d,f). The first new defective lithium structure is presented Figure 6a,b. The globular cluster shown in Figure 6a,b, is similar to those shown in Figure 5 with one important difference: there is no evidence that this cluster was nucleated at an impurity particle. It is not clear if the nucleating impurity particle is not visible due to the resolution limitations of our experimental set up, or if the cluster was formed due to another process such as salt precipitation. The latter possibility is consistent with our observation that such clusters are only observed at the highest salt concentration. The clusters shown in Figures 6c,d are qualitatively different from clusters discussed as far. Here we see a hemispherical cap with lithium globules concentrated on the surface of the cap. The interior of the cap is mostly comprised of the electrolytic phase. The lithium globules in this case are relatively small ranging from 2.3 to 5 µm in

diameter. In Figures 6e,f we show a globule cluster that is similar to the one seen in Figure 6c,d except for the fact that it was not nucleated from an impurity particle (or the nucleating particle was below resolution). Note that at all salt concentrations less than $r = 0.2$, all clusters were seen to nucleate on a detectable impurity particle. The clusters shown in Figure 6 are only obtained in cells that failed quickly (failure was observed in less than 30 cycles).

Previous studies have shown that lithium grain boundaries have shown higher reactivity than the uninterrupted lithium crystal in the presence of liquid electrolytes.[41] A new feature was observed in cells with low salt concentration SEO electrolytes that cycled for a long time (when failure was observed after 90 or more cycles). This feature is shown in Figure 7. A cross section of a failed cell with $r =0.04$ (154 cycles) is shown in Figure 7a. The dark features seen in the cross section correspond to voids, as the electron density in these pixels is much lower than that of lithium metal. These voids were only seen in cells $r = 0.04$ and $r = 0.06$. The top view of this cell, taken at the orange dashed line in Figure 7a, is presented in Figure 7b. Here we observe that voids form hexagonal patterns. It is well known that the grain boundaries in lithium metal have this characteristic shape and dimension[4]. It appears that the voids form over grain boundaries. We thus posit that during cycling, lithium is preferentially stripped from the lithium grain boundaries. For reasons that are not clear, plating is hindered on these regions. We note that some of the voids are buried beneath lithium metal. In addition, the voids are seen at depths as large as 35 µm from the electrolyte/electrode interface. In spite of the fact that only 3.4 µm is cycled. All of the features seen in Figures 5 to 7 extend into the electrode to depths that are much larger than the thickness of the layer of the cycled lithium layer.
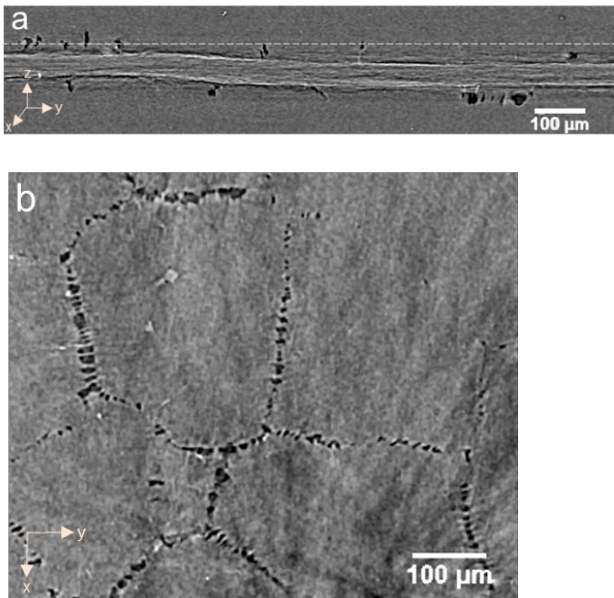
Figure 7. (a) Representative cross-sectional slice through reconstructed X-ray tomograms of lithium-

lithium symmetric cells after cell failure for $r = 0.04$, showing the presence of voids with a darker gray value than lithium close to the electrolyte-electrode interface. (b) Reconstructed X-ray tomography slice into the volume of the lithium from the plane indicated by the orange dashed line in (a) showing the presence of voids at the lithium metal's grain boundaries.

The number of defects (including multiglobular protrusions and mossy lithium) in lithium plating were counted manually by examining all of the tomograms. We have established[27-31] that protrusions nucleate on impurity particles that are randomly distributed in the lithium electrodes. We thus expect comparable numbers of defects from all of the electrodes. We define N_t to be the number of defects observed at the top electrode (where lithium was striped during the first step of the first cycle). Similarly, N_b is the number defects observed at the bottom electrode (where lithium was first plated during the first step of the first cycle). For consistency, the number of defects were determined in one cell, selected at random, for each salt concentration. The fraction of defects on the bottom electrode, F_d, is calculated according equation 1.

$$F_d = \frac{N_b}{N_b + N_t} \quad (1)$$

We expect F_d, to be 0.5. In Figure 8, we plot F_d, versus salt concentration. Surprisingly, F_d, is significantly smaller than 0.5 at all but one salt concentrations. The average value of F_d is 0.19. In 75% of the cells examined, more defects were observed in the top electrode.
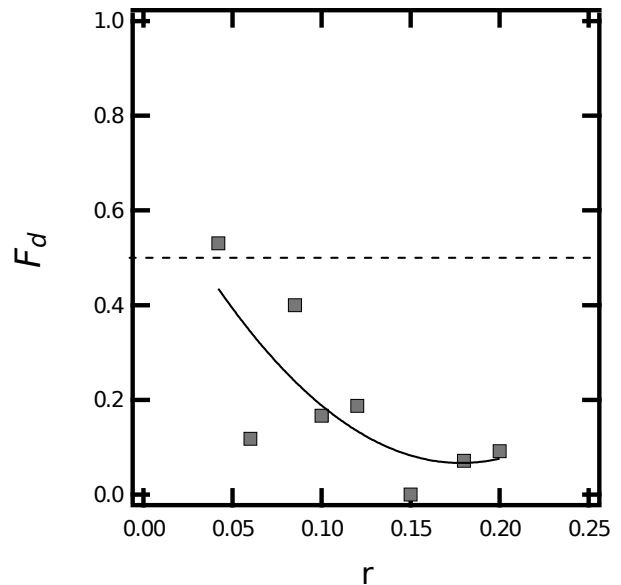
Figure 8 Fraction of defects on the bottom electrode, F_d, as a function of salt concentration, r. One representative cell was chosen for each salt concentration. The dashed line represents a fraction

of 0.5. F_d decreases with increasing salt concentration. The solid curve is to guide the eyes.
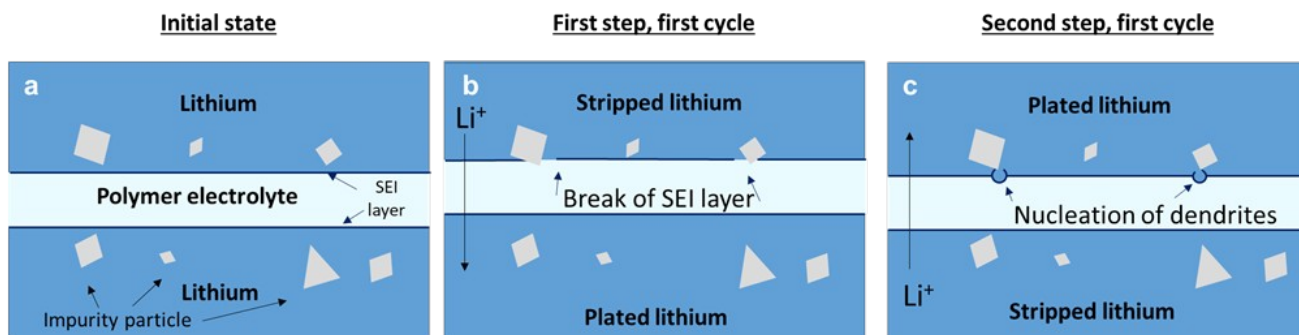

Figure 9. A schematic to explain enhanced density of defects on the electrode that is stripped first in the cycle (top electrode in schematic). (a) Initial state of the lithium-lithium symmetric cell; lithium impurity distribution near the electrode-electrolyte interface is similar in both electrodes. (b) First step of the first cycle. Lithium is stripped from the top electrode and plated to the bottom electrode. Impurity particles are exposed to the electrode-electrolyte interface. This exposes the impurities in the top electrode. (c) Second step of the first cycle. Lithium is stripped from the bottom electrode and plated back to the top electrode, where exposed impurities nucleate lithium protrusions.

A mechanism by which the asymmetry described in Figure 8 may occur is presented schematically in Figure 9. In Figure 9a, we show two lithium electrodes with equal number of impurities near the electrode-electrolyte interfaces. In the first step of the first cycle, a layer of lithium is striped from the top electrode and deposited on the bottom electrode (Figure 9b). This brings the impurities on the top electrode to the electrode-electrolyte interface. In contrast, the impurities in the bottom electrode are buried by the electrodeposited lithium. In the second step of the first cycle, lithium from the bottom electrode is deposited back on the top electrode where the exposed impurities nucleate defects. We posit that the SEI[37] layer is disrupted by insulating impurity particles at the electrode-electrolyte interface and this results in defective lithium plating[28,30]. This results in a higher current near the edges of the particle which, in turn, nucleates lithium globules.

The schematic in Figure 9 provides an explanation for why the electrodeposition in a symmetric lithium-polymer-lithium cell is asymmetric. It is evident that the disparity in defect formation between top and bottom electrodes is likely to be more significant in the early cycles. In other words, we expect cells with short cycle life to exhibit lower values of F_d. This agrees with the data shown in Figure 8, where F_d is seen to decrease more-or-less monotonically with increasing salt concentration. Note that cycle life decreases with increasing salt concentration. The cell with $r = 0.04$ had a cycle life of 154 cycles and F_d is 0.53. In contrast, the cell with $r = 0.2$ had a cycle life of 33 and F_d is 0.09.
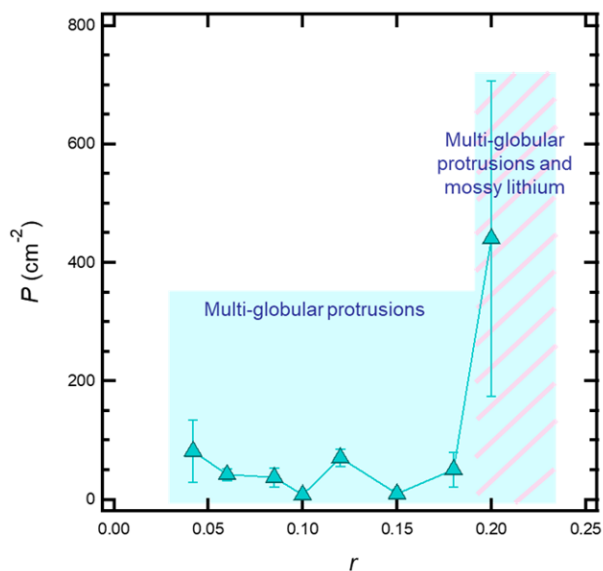

Figure 10. Areal density of defects, P, for each cell versus salt concentration, r. The areal density of defects is more or less constant for $0.04 \leq r \leq 0.18$. Only multiglobular protrusions were observed for these r values. For $r = 0.2$, P increases significantly and globular protrusions and mossy lithium are observed.

Figure 10 is a graph plotting the areal density of defects versus salt concentration. The areal density of defects, P, was obtained by counting the defects in each cell and dividing this number by the cross-sectional area of the imaged portion each cell $S = 0.54$ cm^2. All types of defects were counted. The areal density of defects fluctuates between 8 and 81 defects.cm^{-2} over most of the salt concentration window ($0.04 \leq r \leq 0.18$). This may seems surprising because the lifetime of these cells is a strong function of salt concentration. At the highest salt concentration ($r = 0.2$), the areal defect density

jumps to 440 defects.cm^{-2}. It appears that the nucleation of defects at r = 0.2 is qualitatively different from that at lower salt concentration (also see Figure 6).
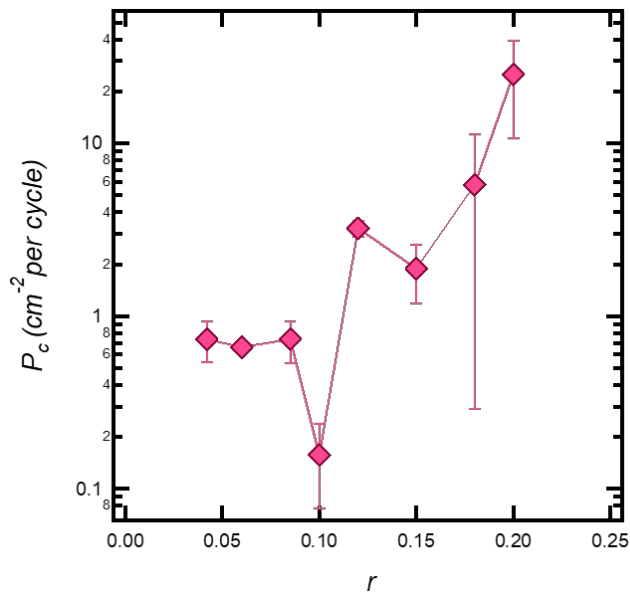

Figure 11. Areal defect density per cycle, P_c, as a function of salt concentration, r. P_c increases with increasing r.The errors reflect the standard deviation in both defects density and cycle life.

It is instructive to examine the areal density of defects per cycle, P_c. This parameter is indicative of the rate of nucleation in defects in our cells. We obtain this parameter by dividing P by cycle life. In Figure 11, we plot P_c versus salt concentration on a semi-log plot. For r ≤ 0.1, P_c is nearly constant at a value of about 1 defect per cm^2 per cycle. Note that the cycle life decreases from 110 to 45 cycles over this concentration range. It appears that the rate of defect nucleation per cycle is roughly constant in the range r < 0.1. We posit that defects formed in this regime are primarily due to impurities in the lithium foil. At higher salt concentration, however P$_c$ increases rapidly with salt concentration, reaching a value as high as 25 cm^{-2} per cycle at r = 0.2. The nucleation of defect in this high salt concentration regime is fundamentally different from that in the low salt concentration regime. We posit that the additional defects formed in this concentration regime is due to changes in the nature of the electrolyte. Because the cycle life decreases monotonically with increasing salt concentration in the high salt concentration regime.

CONCLUSION

We have studied the effect of salt concentration on the morphology of electrodeposited lithium through a rigid block copolymer electrolyte. Lithium-lithium symmetric cells were cycled at fixed current density. Cycle life decreases rapidly with increasing salt concentration. X-ray microtomography reveals the presence of multi-globular protrusions, which are nucleated at

impurity particles. Cell failure is due to the formation of electrolyte-spanning protrusions. In addition, mossy lithium deposits are observed at the highest salt concentration (r = 0.2). In cells with extremely long lifetimes, voids in the electrolyte appear to decorate the grain boundaries in the lithium electrodes. Defects density was found to be higher at the top electrode, the one that was first stripped during cycling as this brings impurity particles to the electrode-electrolyte interface. The areal defect density in failed cells, P, jumps sharply when r is increased from r = 0.18 to 0.2. The areal defect density per cycle, Pc, increases significantly with increasing salt concentration.

There are many potential reasons for our observations that cell lifetime decreases rapidly with increasing salt concentrations. These include changes in mechanical properties, changes in adhesion between the electrolyte and the electrode, changes in electrochemical properties of the electrolyte, and changes in the magnitude of the salt concentration gradients that are obtained during polarization. While much work remains to be done to determine the underpinnings of our observations and develop strategies to mitigate defective electrodeposition, the present study establishes salt concentration as an important parameter that affects nucleation and growth of non-planar electrodeposition of lithium metal through solid polymer electrolytes.

AUTHOR INFORMATION

Corresponding Author

* **E-mail: nbalsara@berkeley.edu. Phone: 1-510-642-8973**

Author Contributions

J.A.M. and W.S.L. synthesized SEO block copolymer. L.F. fabricated samples and performed the experiments. LF, D.Y.P. and J.A.M. aided in synchrotron experimental set-up and discussion of results. L.F. and N.P.B. prepared figures and composed the manuscript. N.P.B. directed the work.
Notes
The authors declare no competing financial interest.

ABBREVIATIONS
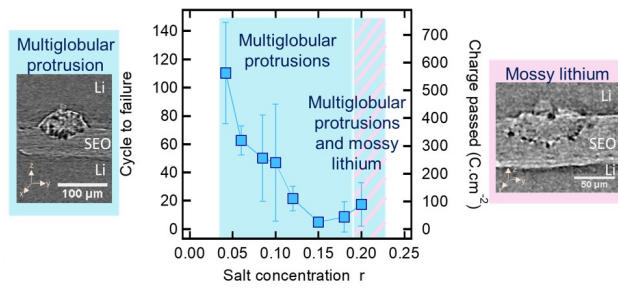
C_d, Charge density passed (C.cm-2); d, Domain spacing (nm); F_d, Fraction of defects on the bottom electrode; i, Applied current density (mA.cm-2); Li, Lithium; Li_2O, Lithium oxide; Li_3N, Lithium nitride;

LiTFSI, Lithium bis (trifluoromethanesulfonyl) imide; *Nb*, Number of defects on the bottom electrode; *NMP*, N-methylpyrrolidone; N_t, Number of defects on the top electrode; *P*, Areal density of defects (cm^{-2});P_c, Areal density of defects per cycle (cm^{-2} per cycle); *PEO*, Poly(ethylene oxide); *PS*, Polystyrene; *r*, Salt concentration; *SEI*, Solid Electrolyte Interphase; *SEO*, Polystyrene-*b*-poly(ethylene) oxide

REFERENCES

(1) Tarascon, J.-M.; Armand, M. Issues and Challenges Facing Rechargeable Lithium Batteries. *Nature* **2001**, *414* (6861), 359–367. https://doi.org/10.1038/35104644.

(2) Thackeray, M. M.; Wolverton, C.; Isaacs, E. D. Electrical Energy Storage for Transportation—Approaching the Limits of, and Going beyond, Lithium-Ion Batteries. *Energy Environ. Sci.* **2012**, *5* (7), 7854–7863. https://doi.org/10.1039/C2EE21892E.

(3) Aurbach, D.; Zinigrad, E.; Cohen, Y.; Teller, H. A Short Review of Failure Mechanisms of Lithium Metal and Lithiated Graphite Anodes in Liquid Electrolyte Solutions. *Solid State Ionics* **2002**, *148* (3), 405–416. https://doi.org/10.1016/S0167-2738(02)00080-2.

(4) Yaws' Handbook of Properties of the Chemical Elements - Knovel https://app.knovel.com/web/toc.v/cid:kpYHPCE007/viewerType:toc.

(5) Whittingham, M. S. Electrical Energy Storage and Intercalation Chemistry. *Science* **1976**, *192* (4244), 1126–1127. https://doi.org/10.1126/science.192.4244.1126.

(6) Selim, R.; Bro, P. Some Observations on Rechargeable Lithium Electrodes in a Propylene Carbonate Electrolyte. *J. Electrochem. Soc.* **1974**, *121* (11), 1457–1459. https://doi.org/10.1149/1.2401708.

(7) Takeda, Y.; Yamamoto, O.; Imanishi, N. Lithium Dendrite Formation on a Lithium Metal Anode from Liquid, Polymer and Solid Electrolytes. *Electrochemistry* **2016**, *84* (4), 210–218. https://doi.org/10.5796/electrochemistry.84.210.

(8) Lin, D.; Liu, Y.; Cui, Y. Reviving the Lithium Metal Anode for High-Energy Batteries. *Nature Nanotechnology* **2017**, *12* (3), 194–206. https://doi.org/10.1038/nnano.2017.16.

(9) Aurbach, D. Review of Selected Electrode–Solution Interactions Which Determine the Performance of Li and Li Ion Batteries. *Journal of Power Sources* **2000**, *89* (2), 206–218. https://doi.org/10.1016/S0378-7753(00)00431-6.

(10) Fenton, D. E.; Parker, J. M.; Wright, P. V. Complexes of Alkali Metal Ions with Poly(Ethylene Oxide). *Polymer* **1973**, *14* (11), 589. https://doi.org/10.1016/0032-3861(73)90146-8.

(11) Armand, M.; Chabagno, J. M.; Duclot, M.; Vashishta, P.; Mundy, J. Fast Ion Transport in Solids, Polymer Electrolytes: Fundamental and Technological Applications; Amsterdam: North Holland, 1979; p 131.

(12) Tarascon, J.-M.; Armand, M. Issues and challenges facing rechargeable lithium batteries https://www.nature.com/articles/35104644 (accessed Mar 23, 2018). https://doi.org/10.1038/35104644.

(13) Lisowska-Oleksiak, A. The Interface between Lithium and Poly(Ethylene-Oxide). *Solid State Ionics* **1999**, *119* (1), 205–209. https://doi.org/10.1016/S0167-2738(98)00504-9.

(14) Armand, M. The History of Polymer Electrolytes. *Solid State Ionics* **1994**, *69* (3), 309–319. https://doi.org/10.1016/0167-2738(94)90419-7.

(15) Bouchet, R.; Maria, S.; Meziane, R.; Aboulaich, A.; Lienafa, L.; Bonnet, J.-P.; Phan, T. N. T.; Bertin, D.; Gigmes, D.; Devaux, D.; Denoyel, D.; Armand, M.. Single-Ion BAB Triblock Copolymers as Highly Efficient Electrolytes for Lithium-Metal Batteries. *Nature Materials* **2013**, *12* (5), 452–457. https://doi.org/10.1038/nmat3602.

(16) Brissot, C.; Rosso, M.; Chazalviel, J.-N.; Baudry, P.; Lascaud, S. In Situ Study of Dendritic Growth Inlithium/PEO-Salt/Lithium Cells. *Electrochimica Acta* **1998**, *43* (10), 1569–1574. https://doi.org/10.1016/S0013-4686(97)10055-X.

(17) Brissot, C.; Rosso, M.; Chazalviel, J.-N.; Lascaud, S. Dendritic Growth Mechanisms in Lithium/Polymer Cells. *Journal of Power Sources* **1999**, *81–82*, 925–929. https://doi.org/10.1016/S0378-7753(98)00242-0.

(18) Dollé, M.; Sannier, L.; Beaudoin, B.; Trentin, M.; Tarascon, J.-M. Live Scanning Electron Microscope Observations of Dendritic Growth in Lithium/Polymer Cells. *Electrochem. Solid-State Lett.* **2002**, *5* (12), A286–A289. https://doi.org/10.1149/1.1519970.

(19) Monroe, C.; Newman, J. Dendrite Growth in Lithium/Polymer Systems A Propagation Model for Liquid Electrolytes under Galvanostatic Conditions. *J. Electrochem. Soc.* **2003**, *150* (10), A1377–A1384. https://doi.org/10.1149/1.1606686.

(20) Monroe, C.; Newman, J. The Effect of Interfacial Deformation on Electrodeposition Kinetics. *J. Electrochem. Soc.* **2004**, *151* (6), A880–A886. https://doi.org/10.1149/1.1710893.

(21) Monroe, C.; Newman, J. The Impact of Elastic Deformation on Deposition Kinetics at Lithium/Polymer Interfaces. *J. Electrochem. Soc.* **2005**, *152* (2), A396–A404. https://doi.org/10.1149/1.1850854.

(22) Wang, C.; Sakai, T.; Watanabe, O.; Hirahara, K.; Nakanishi, T. All Solid-State Lithium-Polymer Battery Using a Self-Cross-Linking Polymer Electrolyte. *J. Electrochem. Soc.* **2003**, *150* (9), A1166–A1170. https://doi.org/10.1149/1.1593652.

(23) Niitani, T.; Shimada, M.; Kawamura, K.; Dokko, K.; Rho, Y.-H.; Kanamura, K. Synthesis of Li + Ion Conductive PEO-PSt Block Copolymer Electrolyte with Microphase Separation Structure. *Electrochem. Solid-State Lett.* **2005**, *8* (8), A385–A388. https://doi.org/10.1149/1.1940491.

(24) Metwalli, E.; Rasool, M.; Brunner, S.; Müller-Buschbaum, P. Lithium-Salt-Containing High-Molecular-Weight Polystyrene-Block-Polyethylene Oxide Block Copolymer Films. *ChemPhysChem* **2015**, *16* (13), 2882–2889. https://doi.org/10.1002/cphc.201500358.

(25) Stone, G. M.; Mullin, S. A.; Teran, A. A.; Hallinan, D. T.; Minor, A. M.; Hexemer, A.; Balsara, N. P. Resolution of the Modulus versus Adhesion Dilemma in Solid Polymer Electrolytes for Rechargeable Lithium Metal Batteries. *J.*

Electrochem. Soc. **2012**, *159* (3), A222–A227. https://doi.org/10.1149/2.030203jes.

(26) Hallinan, D. T.; Mullin, S. A.; Stone, G. M.; Balsara, N. P. Lithium Metal Stability in Batteries with Block Copolymer Electrolytes. *J. Electrochem. Soc.* **2013**, *160* (3), A464–A470. https://doi.org/10.1149/2.030303jes.

(27) Harry, K. J.; Hallinan, D. T.; Parkinson, D. Y.; MacDowell, A. A.; Balsara, N. P. Detection of Subsurface Structures underneath Dendrites Formed on Cycled Lithium Metal Electrodes. *Nature Materials* **2014**, *13* (1), 69–73. https://doi.org/10.1038/nmat3793.

(28) Harry, K. J.; Liao, X.; Parkinson, D. Y.; Minor, A. M.; Balsara, N. P. Electrochemical Deposition and Stripping Behavior of Lithium Metal across a Rigid Block Copolymer Electrolyte Membrane. *J. Electrochem. Soc.* **2015**, *162* (14), A2699–A2706. https://doi.org/10.1149/2.0321514jes.

(29) Harry, K. J.; Higa, K.; Srinivasan, V.; Balsara, N. P. Influence of Electrolyte Modulus on the Local Current Density at a Dendrite Tip on a Lithium Metal Electrode. *J. Electrochem. Soc.* **2016**, *163* (10), A2216–A2224. https://doi.org/10.1149/2.0191610jes.

(30) Maslyn, J. A.; Loo, W. S.; McEntush, K. D.; Oh, H. J.; Harry, K. J.; Parkinson, D. Y.; Balsara, N. P. Growth of Lithium Dendrites and Globules through a Solid Block Copolymer Electrolyte as a Function of Current Density. *J. Phys. Chem. C* **2018**, *122* (47), 26797–26804. https://doi.org/10.1021/acs.jpcc.8b06355.

(31) Schauser, N. S.; Harry, K. J.; Parkinson, D. Y.; Watanabe, H.; Balsara, N. P. Lithium Dendrite Growth in Glassy and Rubbery Nanostructured Block Copolymer Electrolytes. *J. Electrochem. Soc.* **2015**, *162* (3), A398–A405. https://doi.org/10.1149/2.0511503jes.

(32) Bruce, P. G.; Vincent, C. A. Polymer Electrolytes. *J. Chem. Soc., Faraday Trans.* **1993**, *89* (17), 3187–3203. https://doi.org/10.1039/FT9938903187.

(32) Singh, M.; Odusanya, O.; Wilmes, G. M.; Eitouni, H. B.; Gomez, E. D.; Patel, A. J.; Chen, V. L.; Park, M. J.; Fragouli, P.; Iatrou, H.; Hadjichristidis, N.; Cookson, D.; Balsara, N. P. Effect of Molecular Weight on the Mechanical and Electrical Properties of Block Copolymer Electrolytes. *Macromolecules* **2007**, *40* (13), 4578–4585. https://doi.org/10.1021/ma0629541.

(34) Mullin, S. A.; Stone, G. M.; Panday, A.; Balsara, N. P. Salt Diffusion Coefficients in Block Copolymer Electrolytes. *J. Electrochem. Soc.* **2011**, *158* (6), A619–A627. https://doi.org/10.1149/1.3563802.

(35) Cochran, E. W.; Garcia-Cervera, C. J.; Fredrickson, G. H. Stability of the Gyroid Phase in Diblock Copolymers at Strong Segregation. *Macromolecules* **2006**, *39* (7), 2449–2451. https://doi.org/10.1021/ma0527707.

(36) Bates, F. S.; Rosedale, J. H.; Fredrickson, G. H. Fluctuation Effects in a Symmetric Diblock Copolymer near the Order–Disorder Transition. *J. Chem. Phys.* **1990**, *92* (10), 6255–6270. https://doi.org/10.1063/1.458350.

(37) Peled, E. The Electrochemical Behavior of Alkali and Alkaline Earth Metals in Nonaqueous Battery Systems—The Solid Electrolyte Interphase Model. *J. Electrochem. Soc.* **1979**, *126* (12), 2047–2051. https://doi.org/10.1149/1.2128859.

(38) Hewlett, C. W. The Mass Absorption and Mass Scattering Coefficients for Homogeneous X Rays of Wave-Length between 0.13 and 1.05 \AA{}ngstr\"om Units in Water, Lithium, Carbon, Nitrogen, Oxygen, Aluminum, and Iron. *Phys. Rev.* **1921**, *17* (3), 284–301. https://doi.org/10.1103/PhysRev.17.284.

(39) Groso, A.; Stampanoni, M.; Abela, R.; Schneider, P.; Linga, S.; Müller, R. Phase Contrast Tomography: An Alternative Approach. *Appl. Phys. Lett.* **2006**, *88* (21), 214104. https://doi.org/10.1063/1.2207221.

(40) Maia, F.; MacDowell, A.; Marchesini, S.; Padmore, H. A.; Parkinson, D. Y.; Pien, J.; Schirotzek, A.; Yang, C. Compressive Phase Contrast Tomography. In *Image Reconstruction from Incomplete Data VI*; International Society for Optics and Photonics, 2010; Vol. 7800, p 78000F. https://doi.org/10.1117/12.861946.

(41) Gireaud, L.; Grugeon, S.; Laruelle, S.; Yrieix, B.; Tarascon, J.-M. Lithium Metal Stripping/Plating Mechanisms Studies: A Metallurgical Approach. *Electrochemistry Communications* **2006**, *8* (10), 1639–1649. https://doi.org/10.1016/j.elecom.2006.07.037.

For Table of Contents Only